ORIGINAL PAPER

# Leakage Threshold of a Saddle Point

De Huang[1] · Xiang Yan[2] · Roland Larsson[1] · Andreas Almqvist[1]

Abstract
The threshold condition for leakage inception is of great interest to many engineering applications, and it is essential for seal design. In the current study, the leakage threshold is studied by means of a numerical method for a mechanical contact problem between an elastic bi-sinusoidal surface and a rigid flat surface. The coalesce process of the contact patches is first investigated, and a generalized form of solution for the relation between the contact area ratio and the average applied pressure is acquired. The current study shows that the critical value of the average applied pressure and the corresponding contact area required to close the percolation path can be represented as a power law of a shape parameter, if the effect of the hydrostatic load from the pressurized fluid is ignored. With contact patches merged under a constant applied load, the contact breakup process is investigated with elevated sealed fluid pressure condition, and it is shown that the leakage threshold is a function of the excess pressure, which is defined as a ratio between the average applied pressure and the critical pressure under dry contact conditions.

Graphical abstract
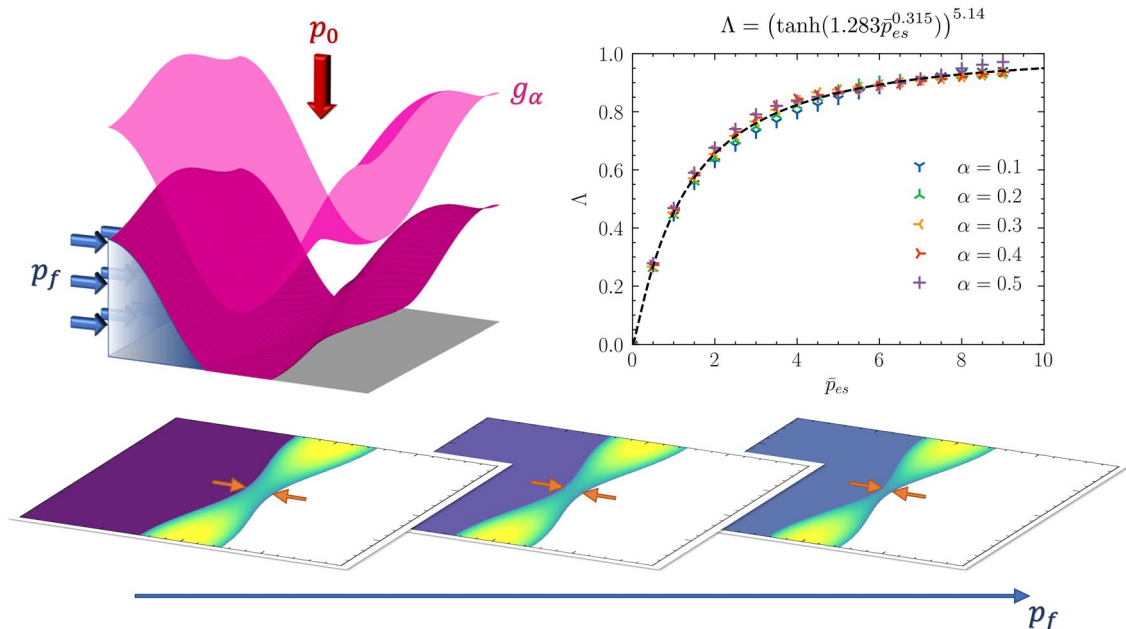
Keywords Seal · Contact mechanics · Leakage · Critical pressure

✉ Andreas Almqvist
  andreas.almqvist@ltu.se

Extended author information available on the last page of the article

List of Symbols

S	Solid–solid contact area
S_f	Flooded area at the high-pressure side
S^*	Critical contact area under the dry condition

S_b	Critical solid–solid contact area when $p_f = p_b$
S_0	Area of the solution domain
p_f	Sealed fluid pressure
Δ	Geometry parameter of the initial gap $g_0(x, y)$
λ	Side length of the square solution domain
ν	Material Poisson ratio
α	Shape parameter of the initial gap $g_0(x, y)$
p	Surface traction (surface stress orthogonal to the contact interface)
p_0	Average applied pressure at vertical direction
p_{saddle}	Surface traction at the saddle point
p_0^*	Critical pressure of dry contact
p_b	Critical pressure of leakage
$\bar{p}_{es}$	Normalized excess pressure defined in Eq. (9)
P_t	Total load at the vertical direction
p_s	Pressure scaling factor
E	Material young's modulus
g_0	Initial gap between the contacting surfaces
g_x	The x-component of g_0
g_y	The y-component of g_0
l_{cx}	Half-width of the rectangular contact strip for g_x
l_{cy}	Half-width of the rectangular contact strip for g_y
p_x^*	Pressure scaling factor for $\bar{p}_x$
p_y^*	Pressure scaling factor for $\bar{p}_y$
β	Partition function for the curve Eq. (3)
ϵ	Error tolerance of p_0
C	Coefficient for Eq. (6)
$c_{0,1,2,3}$	Fitting coefficients for C
$\kappa_{x,y}$	Curvature of $g_0(x, y)$ at the two crest positions

1 Introduction

As a machine element that blocks the fluid flow, the seal achieves its function by compressing two surfaces together and closing the percolation paths between the high- and low-pressure sides. The contact patches are formed when two surfaces are pressed against each other. The initially isolated contact patches for rough surfaces can merge under increased contact load. The fluid leakage is stopped when the connected contact patches isolate the percolation paths between the high- and the low-pressure sides. Since the geometry connectivity of the contact patches decides the transition point of the leakage, it is of great interest to study the coalescence and breakup process of the contact patches.

The early contact mechanics models for the rough surfaces, such as the Greenwood–Williamson model [1] and the Greenwood–Tripp model [2, 3], assumed that the contact between the micro asperities could be decomposed into a group of Hertzian-like contacts and the deformation of each asperity is independent of each other. Since then, both experiments and simulations [4, 5] have shown that even for a simple contact problem between an elastic bi-sinusoidal and

a rigid flat surface, the deformation of the contact patches is not independent of each other, suggesting that the contact patch interaction needs to be considered for the correct contact area, hence, also for the percolation threshold. Elastic contact mechanics accounting for the interaction between contact patches has been developed [6, 7]. It has also been utilized to study the percolation threshold for both the isotropic fractal rough surface and the anisotropic rough surface [8–10]. The contact area ratio at the leakage threshold predicted by both contact mechanics theory and numerical simulations [11–16] is smaller than the value predicted by the bond-percolation theory [17] and the bearing area model [2, 3], because the long-range elastic coupling between contact patches is ignored in the latter two.

Previous research on the leakage threshold of random rough surfaces usually builds on the assumption that the fluid pressure is much smaller than the contact pressure, and that the solid deformation generated by the fluid pressure is negligible. This assumption allows one to decouple the solid contact problem from the fluid leakage problem, and the leakage threshold is determined by the geometry connectivity of the deformed elastic surfaces without the fluid load. There are two situations where the fluid pressure is not negligible. First, the fluid can be trapped between the surface roughness due to the coalescing of the contact patches caused by a increase load. If the trapped fluid is further squeezed by the solid surfaces, its internal pressure will increase due to the volume decrease, thus providing additional load carrying capacity, and preventing further contact between the solid surfaces. Kuznetsov [18, 19] studied the contact problem with fluid entraps in the valleys of a sinusoidal profile. His solution shows that the increased total load can be balanced by the compressed fluid pressure with a constant solid–solid contact length. The experimental findings in [20] have also confirmed that the fluid entrapped between a bi-sinusoidal and a flat surface prevents the further close-up of the gap between them after the adjacent contact patches touch each other. The further increase of the average applied pressure mainly contributes to the deformation near the saddle point, with little variation on the solid–solid contact areas, and the trapped fluid does not leak with its increased hydrostatic pressure [21].

Another situation where the fluid pressure must be considered is when the sealed fluid pressure is comparable with the contact load. It is not a rare case, especially near the boundaries of the contact zones adjacent to the high-pressure side [22]. If there is no leakage, the pressurized fluid from the high-pressure side fills the gap between the contacting surfaces with uniform hydrostatic pressure. The hydrostatic fluid pressure will deform the contacting surfaces and change contact pressure distribution [23]. When the fluid is pressurized from the high-pressure side of an initially sealed system, leakage is observed when the sealed
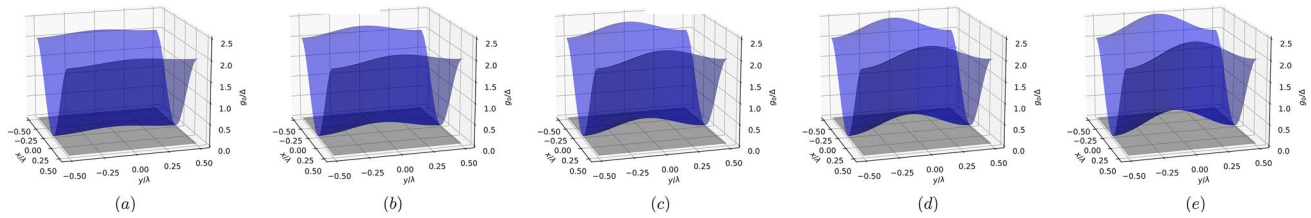
Fig. 1 The initial shape of the elastic bi-sinusoidal surface, mathematically described in Eq. (1), with the shape parameter $\alpha = 0.1$ in (**a**), $\alpha = 0.2$ in (**b**), $\alpha = 0.3$ in (**c**), $\alpha = 0.4$ in (**d**), and $\alpha = 0.5$ in (**e**)

fluid pressure p_f equals the maximum contact pressure [24]. The leakage threshold under this condition is governed by the initial geometries of the contact surfaces, the loading condition, and the sealed fluid pressure.

The contact mechanics problem between an elastic bi-sinusoidal and a rigid flat surface is probably the most simple one that may be used to show the coalescence of the contact patches and the disappearance of the percolation path. Hence, it serves as an important model problem involving the mechanics governing the leakage threshold, which has also been studied in the previous works [4, 5, 12], without considering the fluid load. In this work, we will revisit this problem and extend it to include the effect of the sealed fluid pressure at the high-pressure side. The main research objective here is to investigate the variability of leakage inception with the sealed fluid pressure in initially sealed contacts.

2 Problem Setup

The present study is devoted to the linear elastic contact problem between a non-planar smooth surface in contact with a rigid flat surface. The elastic surface has a initial bi-sinusoidal shape, i.e.,

$$g_0(x,y) = \Delta(1 - \cos(2\pi x/\lambda) + 0.5\alpha(1 + \cos(2\pi y/\lambda))), \quad (1)$$

with $(x,y) \in [-\lambda/2, \lambda/2]^2$, and λ is the side length of the square solution domain. The geometry parameter Δ is chosen as $\Delta = 0.01\lambda$ in the current study to satisfy the small slope requirement of the half-space approximation, while it is noteworthy that the solution in the current study is independent from Δ/λ when normalized with Δ/λ [25]. The shape parameter α controls the initial gap size at the saddle point $(x,y) = (0,0)$, and the gap equals $\alpha\Delta$ under zero loading condition. The initial geometry $g_0(x,y)$ reduces to a 1D cosine profile when $\alpha = 0$. When $\alpha = 2$, the geometry depicted in Eq. (1) is the bi-sinusoidal geometry studied in [4, 5, 12] under a rotation and a translation operation. In the current study, the shape parameter α is chosen as $\alpha = 0.1, 0.2, 0.3, 0.4$ and 0.5, as shown in Fig. 1.

The non-planar smooth surface $g_0(x,y)$ is brought into contact with a rigid flat surface under the total load P_t, and the average applied pressure is $p_0 = P_t/S_0$, with $S_0 = \lambda^2$ the area of the solution domain. The solid–solid contact problem is first studied with the DCD-FFT method [26] (which is a modification of the DC-FFT method with duplicated padding), in which the periodic boundary condition is applied at $y = \pm 0.5\lambda$. With the percolation path being sealed by the coalescence of the two contact patches under constant total load condition, the sealed fluid is filled in from the high-pressure side $x = -0.5\lambda$ with its pressure equaling p_f. Under the elevated p_f condition, the sealed fluid opens up the solid–solid contacts between the surfaces, allowing for the fluid front to move forward to the point that the percolation path is revealed once more, and the leakage is onset. The value of the sealed fluid pressure when the high- and low-pressure sides are first connected is defined as the critical pressure of leakage p_b, and the critical solid–solid contact area when $p_f = p_b$ is denoted as S_b. It is worth to mention that the S_b defined in the current study is not the same as the critical area defined in the studies of [5, 12], in which the deformation of contacting surfaces by the sealed fluid pressure is ignored. The critical contact area under the dry condition is defined as S^* in the current study and the corresponding average applied pressure when the solid–solid contact area S equals S^* is defined as the critical pressure of dry contact, with the notation as p_0^*.

The values of p_0^* are acquired by conducting the contact mechanics simulation under various p_0 conditions, and checking the geometry connectivity of the high- and low-pressure sides with a connected component labeling algorithm [23, 27]. A binary connectivity identifier is defined as 1 when the high- and low-pressure sides are connected, and 0 otherwise. A bisection method is utilized to narrow down the range of the average applied pressure p_0 based on the connectivity identifier, and the simulation is stopped when the range of p_0 is smaller than a specified tolerance $\epsilon = 10^{-3}p_0$, and the critical pressure of dry contact is taken as the lower endpoint of the range of p_0.

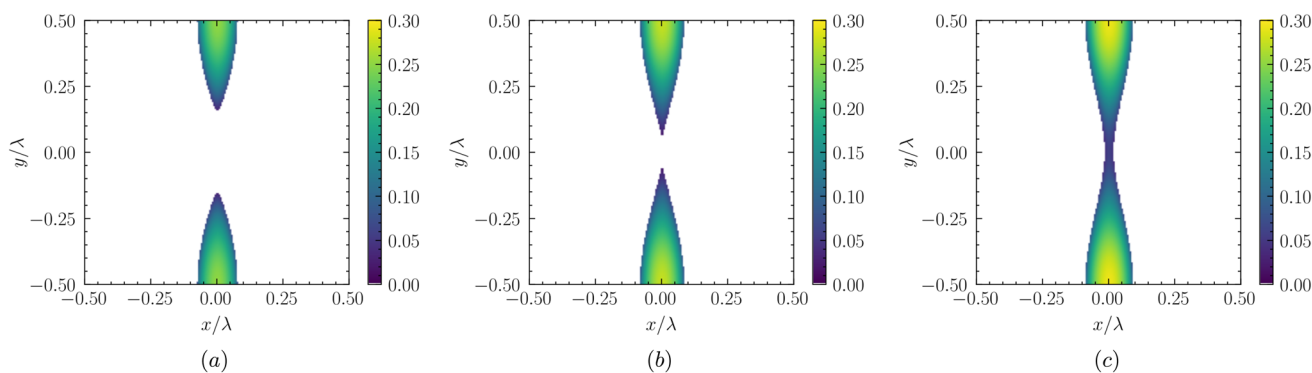The critical pressure of leakage p_b is acquired with a boundary element method developed in [23]. The method

Fig. 2 The surface traction distribution p/p$_s$ under dry contact conditions for the cases of $p_0/p_s = 0.012$ in (**a**), $p_0/p_s = 0.016$ in (**b**) and $p_0/p_s = 0.020$ in (**c**). The shape parameter is $\alpha = 0.3$ and the white regions represent the areas with surface traction equaling zero

is a further development of FFT-accelerated method [28] including the hydrostatic load at the contact interface. The mesh size is chosen as 1024 by 1024. The contact plane geometry tolerance is set to $10^{-5}\Delta$, and the total load tolerance is set to $10^{-9}p_0$ for both the dry contact and the cases with the hydrostatic load.

It is worth to emphasize that the periodic boundary condition is only applied at the y direction in the DCD-FFT method. It differentiates the current study from the previous studies on the bi-sinusoidal surface [4, 5, 12], in which the periodic boundary condition is applied to both the x and y directions. The y–only periodic boundary condition leads to contact pressure concentration when the contact patches touch the corner of the solution domain due to the flat punch effect, and the contact pressure at the corner is unbounded with large value of shape parameter α. So α is set to be $\alpha \in (0.0, 0.5]$ in the current study to avoid the contact pressure singularity under high loading conditions.

3 Results and Discussions

The merging of the two contact patches occurs continuously for non-adhesive solids, without considering the surface deformation by the sealed fluid pressure [12]. Both the critical pressure p_0^* and the critical area S^* under dry contact conditions depend on the shape of the merging contact patches. In this section, the critical quantities p_0^* and S^* are first studied for the initial geometries depicted in Eq. (1) and Fig. 1, followed by the analysis of the critical quantities p_b and S_b with hydrostatic load in consideration. The adhesion force between the contacting surfaces is ignored in the simulation, and the surface tension of the fluid is neglected. The surface stress orthogonal to the contact interface p is referred to as *surface traction* in the discussion below, following the naming convention in [29]. The surface traction p is the contact pressure under dry contact conditions. For

the cases with hydrostatic load, the surface traction p equals the fluid pressure in the fluid-filled regions, and it is the contact pressure at the solid–solid contact regions. Both the force and pressure in the current study are normalized with a pressure scale factor p_s,

$$p_s = \frac{2\pi E}{1 - v^2} \frac{\Delta}{\lambda}, \tag{2}$$

where E is the Young's modulus of the elastic surface, and v is its Poisson ratio.

3.1 Critical Quantities Under the Dry Contact Condition

Figure 2 shows the surface traction distribution p/p_s under dry contact conditions for the initial geometry $g_0(x, y)$ depicted in Eq. (1), with the shape parameter $\alpha = 0.3$. The average applied pressure is $p_0 = 0.012p_s$ in Fig. 2a, $p_0 = 0.016p_s$ in Fig. 2b, and $p_0 = 0.020p_s$ in Fig. 2c. At the
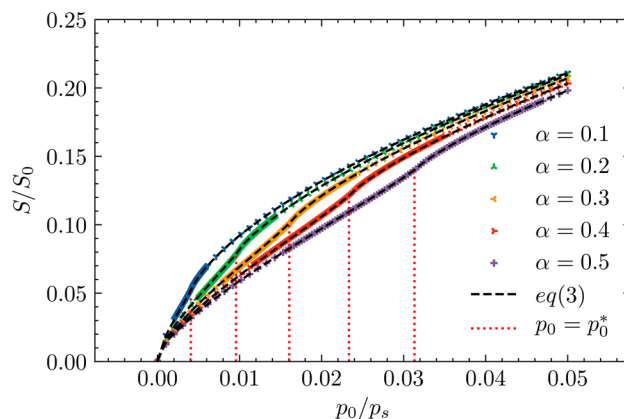

Fig. 3 The relationship between the average applied pressure and the contact area ratio under dry contact conditions
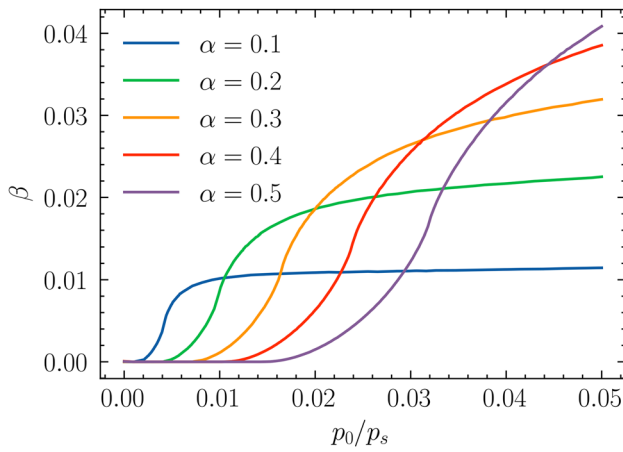
Fig. 4 The partition function β obtained by fitting Eq. (3) to the numerical simulation results shown in Fig. 3

beginning of the contact, the surfaces first touch at the crest positions $(x, y) = (0, \pm 0.5\lambda)$, and the shape of the contact patches can be approximated as two semiellipses. Johnson et al. [4] and Xu et al. [25] have shown that there exists a 2/3 power law between the contact area ratio S/S_0 and the average applied pressure p_0 if the contact patches are semiellipses. The contact area ratio deviates from the 2/3 power law with higher p_0, and it increases as a concave function of the average applied pressure. There is an inflection interval when $p_0 \rightarrow p_0^*$, in which the contact area ratio becomes a convex function of the average applied pressure, as shown in Fig. 3. This inflection interval is firstly discovered by Yastrebov et al. [5] for the isotropic bi-sinusoidal surface, and being confirmed by Xu et al. [25] for the anisotropic bi-sinusoidal surfaces. The contact area ratio transits back to

the concave function of the average applied pressure after p_0 passes p_0^*, and the two contact patches merge together into a dumbbell shape. The size of the dumbbell contact patch, as shown in Fig. 2c, is further increased with elevated p_0.

The relationship between the contact area ratio S/S_0 and average applied pressure p_0/p_s, as shown in Fig. 3, can be fitted into an equation:

$$\frac{S}{S_0} = \frac{2}{\pi}\left(\arcsin\sqrt{(1-\beta)\left(\frac{p_0}{p_S}\right)} + \arcsin\sqrt{\left(\frac{2\beta}{\alpha}\frac{p_0}{p_s}\right)} \right), \quad (3)$$

see Appendix A, where $\beta = \beta(p_0; \alpha)$ is a *partitioning function*. The partitioning function β (obtained by fitting Eq. (3) to the numerical simulation results shown in Fig.
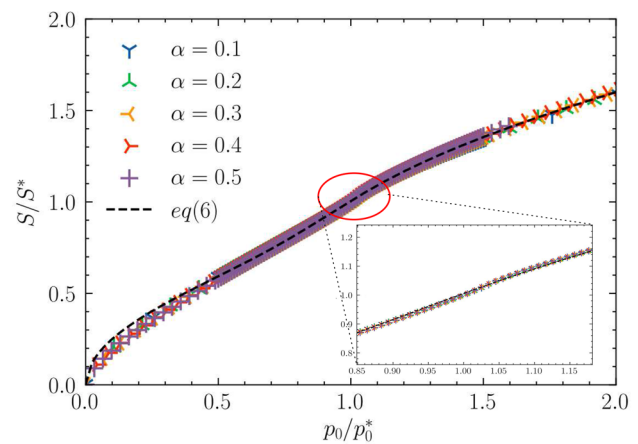

Fig. 6 The relationship between the contact area ratio S and the average applied pressure p_0 under the dry contact conditions, with S normalized with S^* and p_0 normalized with p_0^*
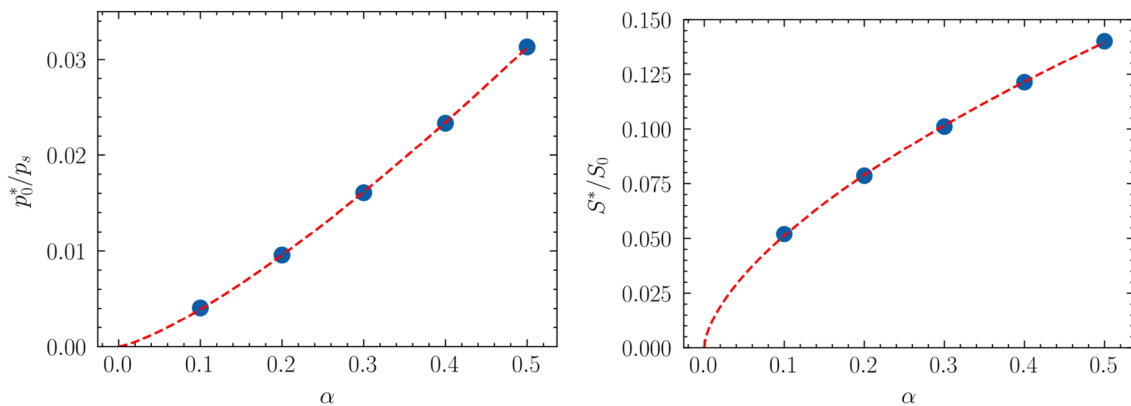

Fig. 5 The critical pressure (left) and critical contact area (right) under dry contact conditions, as function of the shape parameter α. The dots are from simulation and the dashed lines are the power laws Eq. (5)

Table 1 The relative error of Eq. (6)

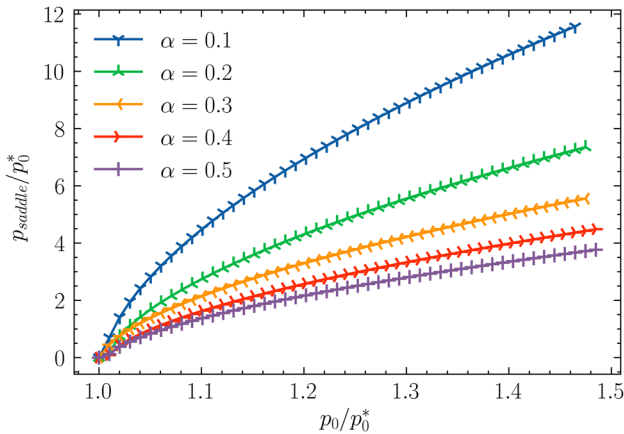| Relative error of Eq. (6)	Average (%)	Maximum (%)
$p_0/p_0^* \in (0, 0.5]$	40.1	319
$p_0/p_0^* \in [0.5, 1.5]$	0.41	2.22
$p_0/p_0^* \in (1.5, 10]$	0.62	1.20

Fig. 7 The surface traction at the saddle point

(3)) is illustrated in Fig. 4. Since the maximum value of β is 0.041 under the current simulation conditions, and $p_0/p_s \in [0, 0.05]$, Eq. (3) can be approximated as

$$\frac{S}{S_0} \approx \frac{2}{\pi} \left(1 + \sqrt{\frac{2\beta}{\alpha}} \right) \sqrt{\frac{p_0}{p_s}}. \tag{4}$$

The critical pressure and the critical contact area under dry condition are represented as a function of the geometry parameter α in Fig. 5. They can be fitted in to the power laws of α, which read

$$\begin{aligned} \frac{p_0^*}{p_s} &= 0.076\alpha^{1.292}, \\ \frac{S^*}{S_0} &= 0.215\alpha^{0.622}. \end{aligned} \tag{5}$$

The power laws Eq. (5) give zero critical pressure and critical contact area ratio under dry contact condition when $\alpha = 0$, this is coinciding with the 1D cosine contact problem, for which there is no percolation paths connecting the high- and low-pressure sides when the loading equals zero.

Substituting the power laws Eq. (5) into Eq. (4) gives

$$\frac{S}{S^*} \approx \frac{2.564}{\pi} \alpha^{0.024} \left(1 + \sqrt{\frac{2\beta}{\alpha}} \right) \sqrt{\frac{p_0}{p_0^*}}$$

$$= \sqrt{C \frac{p_0}{p_0^*}}. \tag{6}$$

The coefficient C can be fitted as

$$C = c_0 + c_1 \arctan \left(c_2 \frac{p_0}{p_0^*} + c_3 \right), \tag{7}$$

with

$$c_0 = 0.943, \quad c_1 = 0.263, \quad c_2 = 3.107, \quad \text{and} \quad c_3 = -2.838. \tag{8}$$

The fitting coefficients c_0 to c_3 are independent from the shape parameter α, as shown in Fig. 6 for $p_0/p_0^* \in (0, 2.0]$. The fitting Eq. (6) agrees well with the simulation results when p_0 is closed to p_0^*, and the average and the maximum relative error of Eq. (6) are shown in Table 1 for different ranges of p_0/p_0^*. While Eq. (6) gives a poor estimation for the solid–solid contact area S when $p_0 \to 0$, the relative error decreases with increased applied load, and the maximum error is less than 2.5% when $p_0/p_0^* > 0.5$.

Equation (6), with the universal coefficients c_0 to c_3 in Eq. (8), suggests that the relationship between the contact area and the average applied pressure, when scaling with their critical values under the dry conditions, is weakly dependent on the initial gap shapes. Utilizing Eq. (6) can significantly simplify the computation of the solid–solid contact area at different loading conditions, and it is of a nature to scale the surface traction p with p_0^*. However, further analysis has shown that the surface traction p/p_0^* at the saddle point $(x, y) = (0, 0)$, after the percolation path is closed, depends on the shape parameter α (Fig. 7). Since the saddle point has the minimum non-zero surface traction after the percolation path closes, its value is closed relative to the hydrostatic pressure required to open up contact. Therefore, the critical pressure of leakage p_b still depends on the initial gap shape.

3.2 Critical Quantities with Hydrostatic Load

Figure 8 shows the surface traction distribution p/p_s for the initial geometry $g_0(x, y)$ depicted in Eq. (1), with the shape parameter $\alpha = 0.4$. The average applied load is $p_0 = 0.04p_s$ in Fig. 8a–c, and the percolation path between the high- and low-pressure sides is disconnected under the dry contact condition. The sealed fluid enters from the low-pressure side $x = -0.5\lambda$ with its pressure equaling p_f, and the value of p_f is $p_f/p_0 = 2.5 \times 10^{-5}$ in Fig. 8a, $p_f/p_0 = 0.285$ in Fig. 8b, and $p_f/p_0 = 0.6125$ in Fig. 8c. The fluid from the high-pressure side filled the gaps between the two contacting surfaces
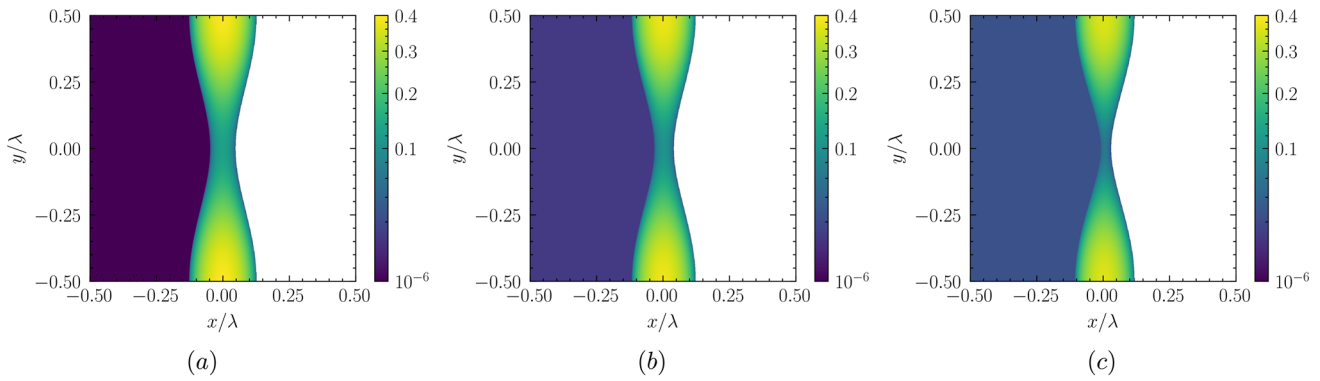
Fig. 8 The surface traction distribution p/p_s for $p_f/p_0 = 2.5 \times 10^{-5}$ in (**a**), $p_f/p_0 = 0.285$ in (**b**), and $p_f/p_0 = 0.6125$ in (**c**). The average applied pressure is $p_0/p_s = 0.04$, and the shape parameter for the initial gap is $\alpha = 0.4$. The white regions represent the areas with surface traction equaling zero

before being blocked by the contact patch. The surface traction distribution in the contact patch and the sealed fluid pressure together determined the fluid front before the contact is open, and the fluid front of the sealed fluid proceeds to the low-pressure side with increased p_f. Since the total load P_t is constant in Fig. 8a–c, the maximum solid–solid contact pressure decreases with increased p_f, and the contact area S is decreased at the same time due to the proceeding of the sealed fluid. The loss of the solid–solid contact happens at both the high- and low-pressure sides, because of the global response of the elastic displacement with the surface traction distribution [23]. The contact patch has a dumbbell shape which is symmetric with $x = 0$ when $p_f = 0$, but loses the symmetry when the sealed fluid pressure increases, because the hydrostatic pressure is only applied at the high-pressure side. Since the neck position of the connected contact patches ($y = 0$) has the smallest surface traction, the contact length at $y = 0$ shrinks the fastest with increased p_f, and the

contact is open along with it when the sealed fluid pressure reaches the critical pressure of leakage p_b.

In the current study, the critical pressure of leakage p_b is defined as the value of the sealed fluid pressure when the high- and low-pressure sides are first connected, so it can only be uniquely determined when $p_0 > p_0^*$. A normalized *excess* pressure $\bar{p}_{es}$ is defined as

$$\bar{p}_{es} = \frac{p_0}{p_0^*} - 1, \tag{9}$$

and the critical pressure of leakage p_b is represented as the function of $\bar{p}_{es}$ for $\bar{p}_{es} \geq 0$, as shown in Fig. 9a. When $\bar{p}_{es} = 0$, the two contact patches touch each other only at the saddle point $(x, y) = (0, 0)$, any infinitesimal fluid pressure can open up the contact and $p_b \approx 0$. The ratio between p_b and the average applied pressure p_0 firstly increases with $\bar{p}_{es}$, and slightly decreases with further growth of $\bar{p}_{es}$. The
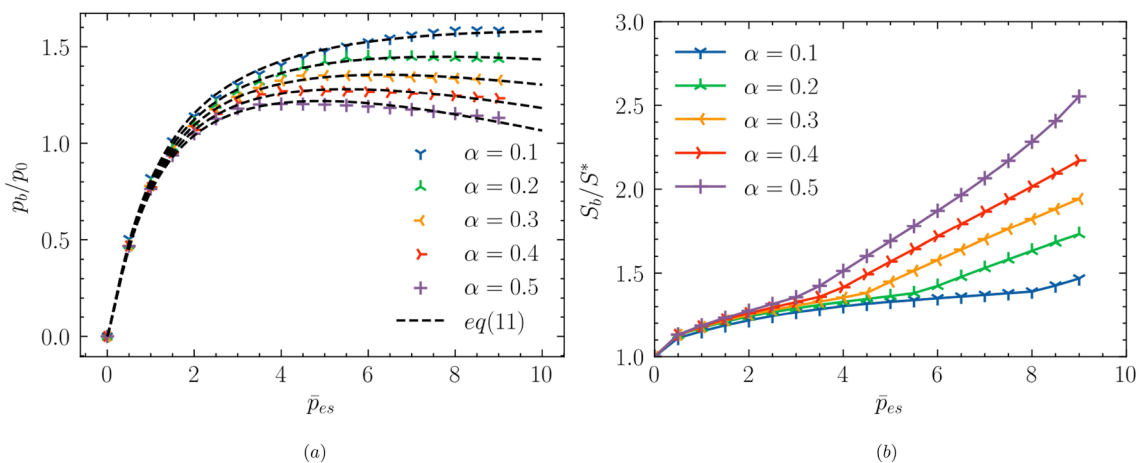

Fig. 9 The critical pressure (**a**) and the critical contact area of leakage (**b**), as the function of the excess pressure defined in Eq. (9)

decrease of p_b/p_0 with the average applied pressure p_0 is consistent with the line contact problem studied in [30]. However, the critical pressure of leakage p_b is always larger than the average applied pressure p_0 in the line contact problem, because the sealed fluid pressure must be increased to the level that all the contact area disappears to reveal the percolation path between the high- and low-pressure sides. On the other hand, the sealed fluid only needs to open up the contact at the saddle point to create leakage for the geometries Eq. (1), so the critical pressure of leakage p_b can be smaller than p_0 in the current study. Another consequence of the existence of the saddle point is that the solid–solid contact area does not need to decrease to zero to initialize the leakage. The critical contact area S_b, which is the solid–solid contact area when the hydrostatic load opens the contact, is non-zero as depicted in Fig. 9b. The critical contact area S_b equals S^* when $\bar{p}_{es} = 0$ for all geometries, since any infinitesimal fluid pressure increases will lead to contact open at the saddle point when $p_0 = p_0^*$. When $p_0 > p_0^*$, the solid–solid contact area S is larger than S^*, and it decreases with the increasing sealed fluid pressure p_f. The remaining solid–solid contact area when the contact is opened is generally higher than S^* in the current study, and it increases with the shape parameter α. The curvatures of $g_0(x, y)$ at the two crest positions ($(x = 0, y = \pm 0.5\lambda)$) are

$$\kappa_x = \frac{4\pi^2 \Delta}{\lambda^2}, \quad \kappa_y = 0.5\alpha \frac{4\pi^2 \Delta}{\lambda^2}, \tag{10}$$

and κ_y increases with α. The higher curvature of the initial gap results in lager maximum contact pressure and steeper contact pressure distribution under the same total load condition, and the fluid front is harder to proceed with elevated hydrostatic pressure [30].
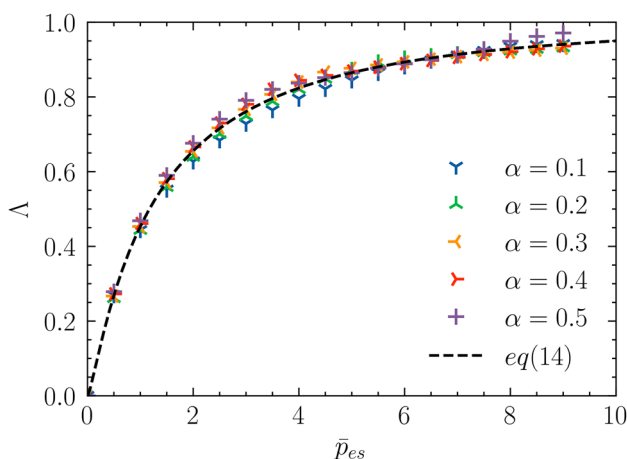
The critical pressure of leakage p_b illustrated in Fig. 9a is fitted into an empirical relationship:

$$\frac{p_b}{p_0} = 2\left(1 - \frac{1}{1 + \bar{p}_{es}}\right)^{1.266} - 0.143\alpha^{0.805}\bar{p}_{es}^{\,0.935}. \tag{11}$$

The relative error generated by Eq. (11) is 0.86% in average and maximize at 3.45%.

To further the understanding of the critical pressure ratio p_b/p_0, a dimensionless parameter Λ is introduced as the critical pressure factor as follows [30]:

$$\Lambda = \left(\frac{S_f + S}{S_0}\right)\frac{p_b}{p_0}, \tag{12}$$

with S_f the flooded area at the high-pressure side when the sealed fluid pressure $p_f = 0$ and the average applied pressure $p_0 > p_0^*$. Due to the symmetry of the current problem under the dry contact condition, the S_f can be written as

$$\frac{S_f}{S_0} = \frac{1}{2}\left(1 - \frac{S}{S_0}\right). \tag{13}$$

The critical pressure factor Λ is plotted against the excess pressure $\bar{p}_{es}$ in Fig. 10, and it is fitted into an empirical relationship, viz.

$$\Lambda = \left(\tanh(1.283\bar{p}_{es}^{\,0.315})\right)^{5.14}. \tag{14}$$

The fitting coefficients in Eq. (14) are independent from the shape parameter α. Substituting Eq. (14) into Eq. (12) allows one to calculate the critical pressure ratio p_b/p_0 with S and $\bar{p}_{es}$, which are quantities available from the dry contact simulation. The relative error of p_b/p_0 generated from Eq. (14) is 1.48% in average, when comparing with the simulation results, and the maximum relative error is 4.61%.

4 Conclusions

A contact problem between a geometrically anisotropic bi-sinusoidal surface and a rigid flat surface is revisited in the current paper. The critical pressure and the critical solid–solid contact area are of main research interest since they are closely related to the leakage inception. The critical quantities are first studied without considering the hydrostatic load of the pressurized fluid. The relationship between the solid–solid contact area and the average applied load acquired from the current study qualitatively agrees with the previous studies from other researchers, and the detailed transition regime of the contact area is also observed. Instead of studying the asymptotic solution of this contact problem, a generalized form of solution Eq. (3) is constructed based on Westergaard's solution of the 1D cosine contact. By introducing a partition function $\beta(p_0; \alpha)$,

Fig. 10 The critical pressure factor, as the function of the excess pressure

Eq. (3) can fit the contact area with high accuracy for a wide range of shapes and loading conditions. Moreover, it is found that the relationship between the contact area and the average applied pressure, when normalized with their critical quantities, is independent of the shape parameter.

The critical pressure and critical contact area for leakage are further studied by first applying a load to close the saddle point, and then filling the contact interface with fluid from the high-pressure side. The contact is lost due to increased sealed fluid pressure, and it was discovered that the sealed fluid pressure required to open up the contact and the remaining solid–solid contact area before the revealing of the percolation path can be represented as a function of excess pressure, which is defined as the difference between the applied pressure and the critical pressure under dry contact conditions. On top of that, a dimensionless parameter, called the critical pressure factor, is defined based on the previous studies from the same authors. It is shown that the critical pressure factor, when represented as a function of the excess pressure, is independent from the shape of the initial geometries. Utilizing the critical factor allows one to acquire the critical pressure for

leakage using the quantities from the dry contact simulations, which are well studied and easily accessible from the previous research.

Appendix A. The relation between the contact area ratio and the average applied pressure under dry contact condition

The contact area S is a continuous function of the average applied pressure p_0 for non-adhesive elastic contact [12], and it depends on the geometries of the contact surfaces. Hence, the ratio of the contact area to the nominal area can be formulated as

$$\frac{S}{S_0} = f(p_0;\alpha), \tag{A.1}$$

where (the continuous function) $f(p_0;\alpha)$ should satisfy that:
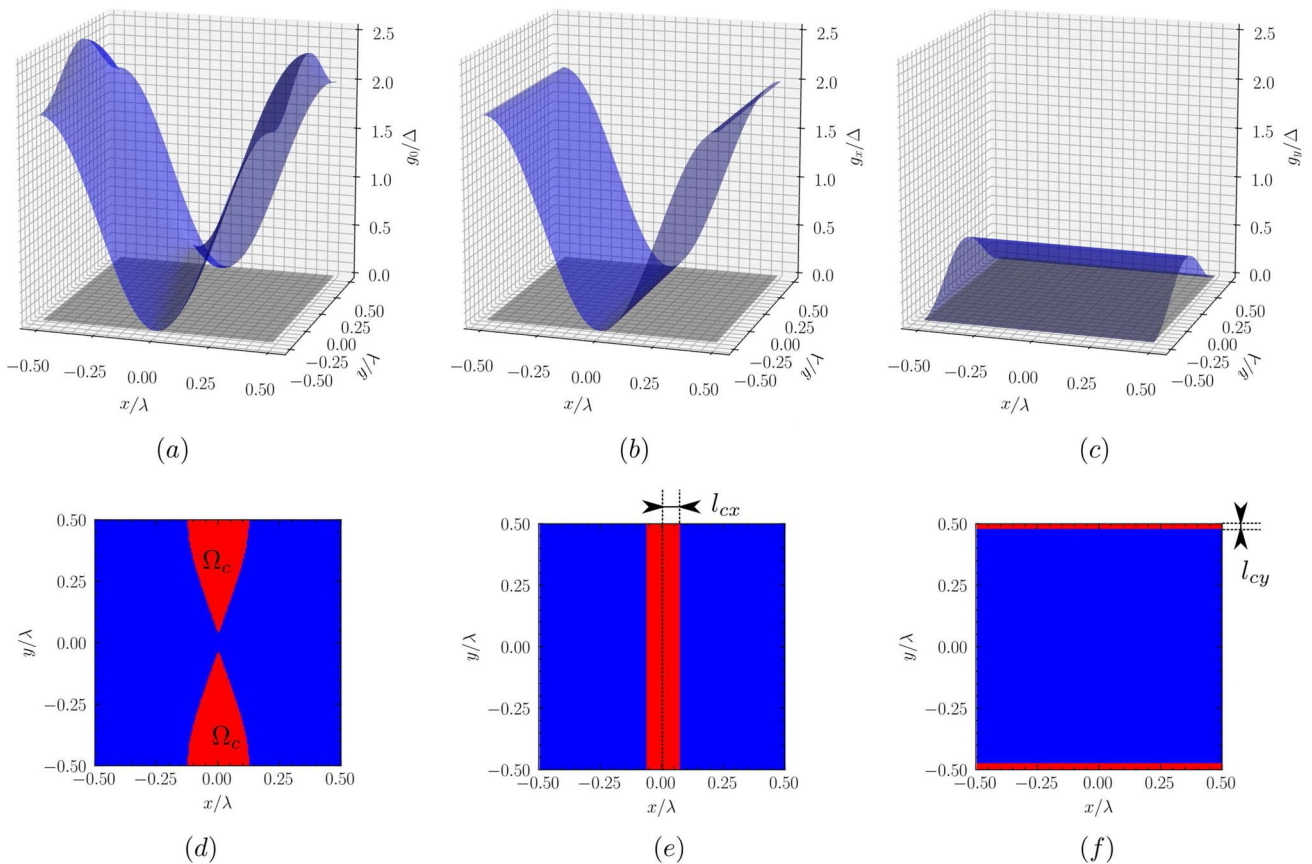
$$f(0;\alpha) = 0, \tag{A.2}$$

Fig. 11 Top row: the initial elastic surface $g_0(x,y)$ with the shape parameter $\alpha = 0.5$ (**a**), the surface $g_x(x)$ depicted in eq. (A.4) (**b**), and the surface $g_y(y)$ depicted in eq. (A.5), with $\alpha = 0.5$ (**c**). Bottom row: the schematic view of the contact region for the initial geom-

etry depicted in (**a**)-(**c**) contacts with a flat rigid surface. The contact region is colored in red, and the initial elastic surface is $g_0(x,y)$ in (**d**), $g_x(x,y)$ in (**e**) and $g_y(y)$ in (**f**)

for any value of α (the shape parameter that controls the initial gap size at the saddle point $(x, y) = (0, 0)$) because the contact area is zero when there is no applied load.

In the current problem, the initial gap $g_0(x, y)$ in eq. (1) can be written as:

$$g_0(x, y) = g_x(x) + g_y(y), \tag{A.3}$$

with

$$g_x(x) = \Delta(1 - \cos(2\pi x/\lambda)), \tag{A.4}$$

and

$$g_y(y) = 0.5\alpha\Delta(1 + \cos(2\pi y/\lambda)). \tag{A.5}$$

When $\alpha \to 0$, $g(x, y) \to g_x(x)$, the contact area S is a rectangular strip of shape $2l_{cx} \times \lambda$, as shown in Fig. 11 (e). The values of l_{cx}, according to the 1D Westergaard's solution [31], is:

$$l_{cx} = \frac{\lambda}{\pi} \arcsin \sqrt{\frac{p_0}{p_x^*}}, \tag{A.6}$$

with

$$p_x^* = \frac{\pi E}{1 - \nu^2} \frac{\Delta}{\lambda} = \frac{p_s}{2}. \tag{A.7}$$

Therefore,

$$\left.\frac{S}{S_0}\right|_{\alpha=0} = f(p_0; 0) = \frac{2}{\pi} \arcsin \sqrt{\frac{2p_0}{p_s}}. \tag{A.8}$$

When $\alpha \to \infty$, $g(x, y) \approx g_y(y)$, and the contact area S is a rectangular strip of shape $2\lambda \times l_{cy}$ as shown in Fig. 11 (f). The values of l_{cy}, according to the 1D Westergaard's solution [31], is:

$$l_{cy} = \frac{\lambda}{\pi} \arcsin \sqrt{\frac{p_0}{p_y^*}}, \tag{A.9}$$

with

$$p_y^* = \frac{\pi E}{1 - \nu^2} \frac{0.5\alpha\Delta}{\lambda} = 0.25\alpha p_s. \tag{A.10}$$

Therefore,

$$\left.\frac{S}{S_0}\right|_{\alpha\to\infty} = f(p_0; \infty) = \frac{2}{\pi} \arcsin \sqrt{\frac{4p_0}{\alpha p_s}}. \tag{A.11}$$

It is assumed that when $\alpha \in (0, \infty)$, the relation between contact area and average applied pressure eq. (A.1) can be reconstructed through function composition:

$$f(p_0; \alpha) = \frac{1}{2}(f(f_1(p_0; \alpha)p_0; 0) + f(f_2(p_0; \alpha)p_0; \infty)). \tag{A.12}$$

The factor $\frac{1}{2}$ is applied in eq. (A.12) to normalize the contact area ratio, which is always less or equal to one. For the reconstruction to satisfy eq. (A.8) and eq. (A.11), one must have:

$$f(f_1(p_0; 0)p_0; 0) = 2f(p_0; 0), \quad f_2(p_0; 0) = 0, \tag{A.13a}$$

$$f_1(p_0; \infty) = 0, \quad f(f_2(p_0; \infty)p_0; \infty) = 2f(p_0; \infty). \tag{A.13b}$$

Because the small values of p_0 in the current study, the function f can be approximated linearly, and eqs. (A.13a) and (A.13b) can be written as:

$$f_1(p_0; 0) = 2, \quad f_2(p_0; 0) = 0, \tag{A.14a}$$

$$f_1(p_0; \infty) = 0, \quad f_2(p_0; \infty) = 2. \tag{A.14b}$$

One way to satisfy both eqs. (A.14a) and (A.14b) is by choosing f_1 and f_2 so that

$$f_1(p_0; \alpha) + f_2(p_0; \alpha) = 2, \tag{A.15}$$

which can be achieved by introducing a *partitioning function* β and letting

$$f_2(p_0; \alpha) = 2\beta(p_0; \alpha), \quad f_1(p_0, \alpha) = 2 - 2\beta(p_0; \alpha). \tag{A.16}$$

By substituting eq. (A.16) into eq. (A.12), and then using eq. (A.8) and eq. (A.11) gives:

$$\begin{aligned} \frac{S}{S_0} &= f(p_0; \alpha) = \frac{1}{\pi}\left(\arcsin \sqrt{(2 - 2\beta)\left(\frac{2p_0}{p_s}\right)} + \arcsin \sqrt{\left(\frac{8\beta}{\alpha}\frac{p_0}{p_s}\right)} \right) \\ &\approx \frac{2}{\pi}\left(\arcsin \sqrt{(1 - \beta)\left(\frac{p_0}{p_s}\right)} + \arcsin \sqrt{\left(\frac{2\beta}{\alpha}\frac{p_0}{p_s}\right)} \right). \end{aligned} \tag{A.17}$$

It is worth mentioning that eq. (A.12) is not the only way to reconstruct $f(p_0;\alpha)$, e.g.,

$$f(p_0;\alpha) = h_1(p_0;\alpha)f(p_0;0) + h_2(p_0;\alpha)f(p_0;\infty), \tag{A.18}$$

with

$$h_1(p_0;\alpha = 0) = 1, \quad h_2(p_0;\alpha = 0) = 0, \tag{A.19a}$$

$$h_1(p_0;\alpha \to \infty) = 0, \quad h_2(p_0;\alpha \to \infty) = 1, \tag{A.19b}$$

also satisfies eq. (A.8) and eq. (A.11). However, the numerical experiment shows that the fitting equation based on eq. (A.18) gives a poor result with the current simulation data.

Author Contributions All authors have been working on the conception and design of the work, model development, analyzing the results, and writing and reviewing the manuscript. The first author, DH, stands for the major contribution to all parts and was also the one developing the numerical solution procedure and running the simulations.

Declarations

Conflict of interest The authors declare that they have no known competing financial interests or personal relationships that could have appeared to influence the work reported in this paper.

References

1. Greenwood, J.A., Williamson, J.P.: Contact of nominally flat surfaces. Proc. R. Soc. Lond. Ser. A **295**(1442), 300–319 (1966)
2. Greenwood, J.A., Tripp, J.H.: The elastic contact of rough spheres. J. Appl. Mech. **34**(1), 153–159 (1967). https://doi.org/10.1115/1.3607616
3. Greenwood, J.A., Tripp, J.: The contact of two nominally flat rough surfaces. Proc. Inst. Mech. Eng. **185**(1), 625–633 (1970)
4. Johnson, K., Greenwood, J., Higginson, J.: The contact of elastic regular wavy surfaces. Int. J. Mech. Sci. **27**(6), 383–396 (1985)
5. Yastrebov, V.A., Anciaux, G., Molinari, J.-F.: The contact of elastic regular wavy surfaces revisited. Tribol. Lett. **56**(1), 171–183 (2014)
6. Persson, B.N.: Contact mechanics for randomly rough surfaces. Surf. Sci. Rep. **61**(4), 201–227 (2006)
7. Almqvist, A., Campana, C., Prodanov, N., Persson, B.N.: Interfacial separation between elastic solids with randomly rough surfaces: comparison between theory and numerical techniques. J. Mech. Phys. Solids **59**(11), 2355–2369 (2011)
8. Persson, B.N.: Interfacial fluid flow for systems with anisotropic roughness. Eur. Phys. J. E **43**, 1–11 (2020)
9. Persson, B.N., Yang, C.: Theory of the leak-rate of seals. J. Phys. Condens. Matter **20**(31), 315011 (2008)
10. Persson, B.N., Prodanov, N., Krick, B., Rodriguez, N., Mulakaluri, N., Sawyer, W., Mangiagalli, P.: Elastic contact mechanics: percolation of the contact area and fluid squeeze-out. Eur. Phys. J. E **35**(1), 1–17 (2012)
11. Dapp, W.B., Lücke, A., Persson, B.N., Müser, M.H.: Self-affine elastic contacts: percolation and leakage. Phys. Rev. Lett. **108**(24), 244301 (2012)
12. Dapp, W.B., Müser, M.H.: Contact mechanics of and Reynolds flow through saddle points: on the coalescence of contact patches and the leakage rate through near-critical constrictions. EPL (Europhys. Lett.) **109**(4), 44001 (2015)
13. Dapp, W.B., Müser, M.H.: Fluid leakage near the percolation threshold. Sci. Rep. **6**(1), 1–8 (2016)
14. Wang, A., Müser, M.H.: Percolation and Reynolds flow in elastic contacts of isotropic and anisotropic, randomly rough surfaces. Tribol. Lett. **69**(1), 1–11 (2021)
15. Yang, Z., Ding, X., Liu, J., Zhang, F.: Effect of the finite size of generated rough surfaces on the percolation threshold. Proc. Inst. Mech. Eng. C J. Mech. Eng. Sci. **233**(16), 5897–5902 (2019)
16. Putignano, C., Afferrante, L., Carbone, G., Demelio, G.P.: A multiscale analysis of elastic contacts and percolation threshold for numerically generated and real rough surfaces. Tribol. Int. **64**, 148–154 (2013)
17. Kesten, H.: Percolation Theory for Mathematicians, vol. 194. Springer, New York (1982)
18. Kuznetsov, Y.A.: Effect of fluid lubricant on the contact characterics of rough elastic bodies in compression. Wear **102**(3), 177–194 (1985). https://doi.org/10.1016/0043-1648(85)90217-0
19. Kuznetsov, E.A.: Superposition principle in the solution of contact problems with allowance for friction. Sov. Appl. Mech. **14**(5), 494–498 (1978). https://doi.org/10.1007/bf00883876
20. Matsuda, K., Hashimoto, D., Nakamura, K.: Real contact area and friction property of rubber with two-dimensional regular wavy surface. Tribol. Int. **93**, 523–529 (2016)
21. Shvarts, A.G.: Coupling mechanical frictional contact with interfacial fluid flow at small and large scales. Ph.D. thesis, Université Paris sciences et lettres (2019)
22. Shvarts, A.G., Yastrebov, V.A.: Fluid flow across a wavy channel brought in contact. Tribol. Int. **126**, 116–126 (2018)
23. Huang, D., Yan, X., Larsson, R., Almqvist, A.: Boundary element method for the elastic contact problem with hydrostatic load at the contact interface. Appl. Surf. Sci. Adv. **6**, 100176 (2021)
24. Liu, Q., Wang, Z., Lou, Y., Suo, Z.: Elastic leak of a seal. Extreme Mech. Lett. **1**, 54–61 (2014)
25. Xu, Y., Rostami, A., Jackson, R.L.: Elastic contact between a geometrically anisotropic bisinusoidal surface and a rigid base. J. Tribol. **137**(2), 021402 (2015)
26. Chen, W.W., Liu, S., Wang, Q.J.: Fast fourier transform based numerical methods for elasto-plastic contacts of nominally flat surfaces. J. Appl. Mech. **75**(1), 011022 (2008). https://doi.org/10.1115/1.2755158
27. Wu, K., Otoo, E., Shoshani, A.: Optimizing connected component labeling algorithms. Med. Imaging **5747**, 1965–1976 (2005)
28. Liu, S., Wang, Q., Liu, G.: A versatile method of discrete convolution and fft (dc-fft) for contact analyses. Wear **243**(1–2), 101–111 (2000)
29. Johnson, K.L.: Contact Mechanics. Cambridge University Press, Cambridge (1987)

30. Huang, D., Yan, X., Larsson, R., Almqvist, A.: The critical pressure for bulk leakage of non-planar smooth surfaces. Tribol. Lett. **70**(3), 1–14 (2022)

31. Westergaard, H.M.: Bearing pressure and cracks. ASME J. Appl. Mech. **6**, 49–53 (1939)

Authors and Affiliations

De Huang[1] · Xiang Yan[2] · Roland Larsson[1] · Andreas Almqvist[1]

[1]　Division of Machine Elements, Luleå University of Technology, 97187 Luleå, Sweden

[2]　Saint-Gobain, Bristol, RI 02809, USA